ARTICLES
https://doi.org/10.1038/s41563-019-0317-4
nature materials

Pressure promoted low-temperature melting of metal–organic frameworks

Remo N. Widmer[1], Giulio I. Lampronti[1], Simone Anzellini[2], Romain Gaillac[3], Stefan Farsang[1], Chao Zhou[4], Ana M. Belenguer[5], Craig W. Wilson[6], Hannah Palmer[7], Annette K. Kleppe[2], Michael T. Wharmby[2,8], Xiao Yu[9], Seth M. Cohen[9], Shane G. Telfer[10], Simon A. T. Redfern[1], François-Xavier Coudert[3], Simon G. MacLeod[6,11] and Thomas D. Bennett[7]*

Metal–organic frameworks (MOFs) are microporous materials with huge potential for chemical processes. Structural collapse at high pressure, and transitions to liquid states at high temperature, have recently been observed in the zeolitic imidazolate framework (ZIF) family of MOFs. Here, we show that simultaneous high-pressure and high-temperature conditions result in complex behaviour in ZIF-62 and ZIF-4, with distinct high- and low-density amorphous phases occurring over different regions of the pressure–temperature phase diagram. In situ powder X-ray diffraction, Raman spectroscopy and optical microscopy reveal that the stability of the liquid MOF state expands substantially towards lower temperatures at intermediate, industrially achievable pressures and first-principles molecular dynamics show that softening of the framework coordination with pressure makes melting thermodynamically easier. Furthermore, the MOF glass formed by melt quenching the high-temperature liquid possesses permanent, accessible porosity. Our results thus imply a route to the synthesis of functional MOF glasses at low temperatures, avoiding decomposition on heating at ambient pressure.

The discovery of a growing family of over 60,000 metal–organic framework (MOF) and coordination polymer compounds[1] demonstrates the chemical versatility of these functional microporous materials. Their high surface areas, generated by regular arrays of metal nodes connected by organic ligands, has led to proposed applications in water harvesting[2], gas storage[3], gas separation[4] and catalysis[5]. Research in this field has focused predominantly on ordered, crystalline MOF materials. However, there is growing recognition of other unusual physical properties in this family of 'soft crystals'[6], with examples including defects[7], framework flexibility[8] and disorder[9], that extend our appreciation of the impact of MOF materials[10]. A rich set of structural responses to external forces has been uncovered[11], including negative gas adsorption[12], breathing[13] and temperature[14] (T)- or pressure (P)-induced phase transitions[15]. Much still remains to be discovered about MOFs, especially with respect to their dynamic behaviour.

Similar to MOFs, silicates and other minerals display a wide diversity of interesting physical behaviours, particularly at non-ambient conditions. For example, studies of stability boundaries and properties in P–T space are well established[16]: SiO_2 shows seven crystalline polymorphs[17], numerous metastable porous phases, two polyamorphs[18] and a complex melting curve at high-P, high-T conditions. Despite apparent chemical differences, MOFs find analogues in the mineral world[19]. For example, metal oxalate MOFs[20,21] are synthetic analogues of two minerals[22], stepanovite [$NaMgFe(C_2O_4)_3 \cdot 8\text{-}9H_2O$] and zhemchuzhnikovite [$NaMg(Fe_{0.4}Al_{0.6})(C_2O_4)_3 \cdot 8\text{-}9H_2O$]. Topological similarities are also known, for example between zeolites, which are based on tetrahedral SiO_4 and AlO_4 units, and zeolitic imidazolate frameworks (ZIFs), an important subgroup of MOFs[23] that forms low-density networks based on tetrahedral units of ZnN_4. Both ZIFs[24,25] and zeolites[26,27] retain their microporosity even at relatively high P and T. Even higher P and T conditions ultimately induce phase transitions[28–31] and melting[32]. The glasses formed from such MOF liquids[33] represent a new class of melt-quenched glass materials formed of amorphous, SiO_2-like, continuous random networks[34]. Moreover, these glasses inherit the chemical connectivity and composition of their parent MOF. Understanding the formation of MOF glasses via solid-state conversion or melt quenching is thus of great importance[32,34]. The glass formed from ZIF-62 has been shown to exhibit substantial resistance to crystallization[35], whereas those formed from other ZIFs have recently been demonstrated to show permanent, accessible porosity[36]. Alongside their unique internal structures, MOF glasses and liquids are of great interest as they provide a route to manufacturing complex, monolithic glassy MOF objects from MOF powders by melt-casting[32] and hot-pressing[37].

The separate P- and T-dependent studies carried out on ZIFs, alongside investigations of the behaviour of the liquid MOF phase at higher pressures, motivated us to construct a P–T phase diagram of this MOF system. We selected ZIF-62 [$Zn(Im)_{1.75}(bIm)_{0.25}$] (where Im is imidazolate, $C_3H_3N_2^-$ and bIm is benzimidazolate, $C_7H_5N_2^-$) due to its known stable liquid state, which occurs between the melting temperature of approximately 430 °C, and a decomposition temperature of approximately 500 °C (ref. [32]). ZIF-62 crystallizes in the

[1]Department of Earth Sciences, University of Cambridge, Cambridge, UK. [2]Diamond Light Source Ltd, Harwell Science and Innovation Campus, Didcot, UK. [3]Chimie ParisTech, PSL University, CNRS, Institut de Recherche de Chimie Paris, Paris, France. [4]Department of Chemistry and Bioscience, Aalborg University, Aalborg, Denmark. [5]Department of Chemistry, University of Cambridge, Cambridge, UK. [6]Atomic Weapons Establishment, Aldermaston, UK. [7]Department of Materials Sciences & Metallurgy, University of Cambridge, Cambridge, UK. [8]Deutsches Elektronen-Synchrotron (DESY), Hamburg, Germany. [9]Department of Chemistry and Biochemistry, University of California, San Diego, La Jolla, CA, USA. [10]MacDiarmid Institute for Advanced Materials and Nanotechnology, Institute of Fundamental Sciences, Massey University, Palmerston North, New Zealand. [11]SUPA, School of Physics & Astronomy, and Centre for Science at Extreme Conditions, University of Edinburgh, Edinburgh, UK. *e-mail: tdb35@cam.ac.uk

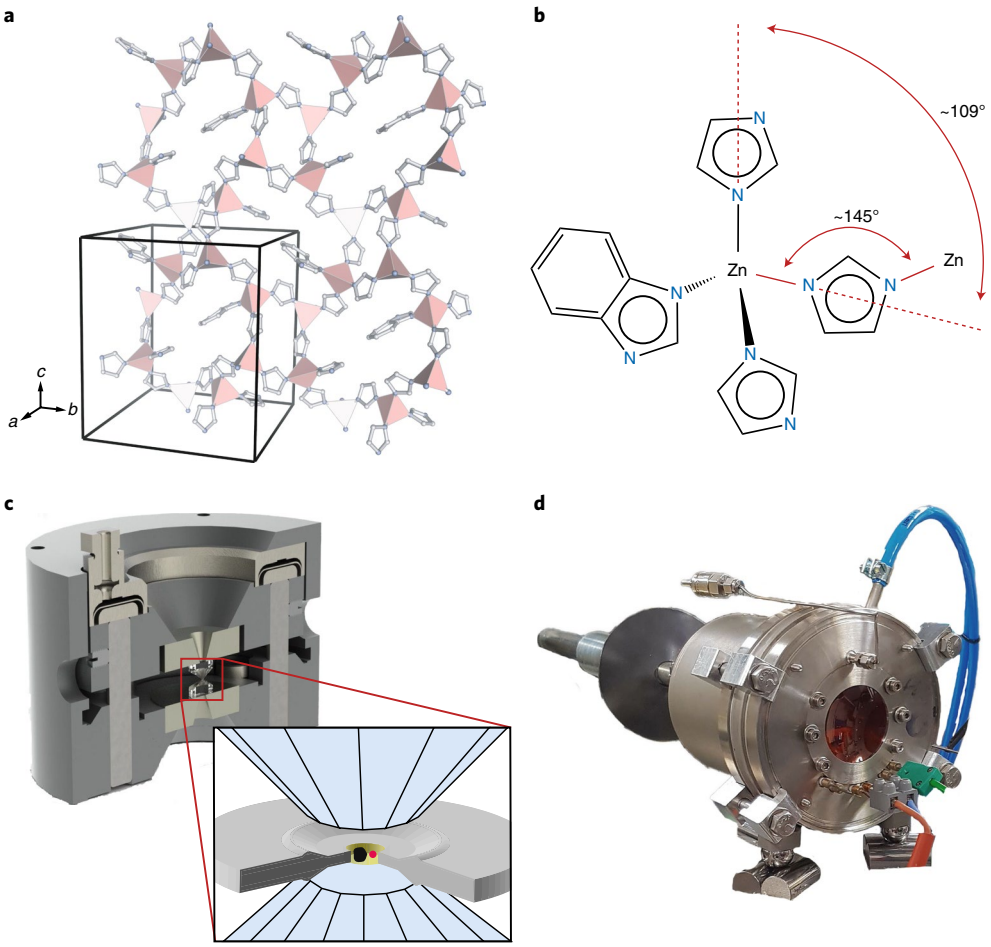

Fig. 1 | Crystal structure of ZIF-62 and experimental set-up. a, Representative slice of the ZIF-62 structure (N, light blue; C, white; ZnN_4 tetrahedra, pink) perpendicular to the *a* axis, revealing the main connectivity of eight- and four-membered-rings. For clarity, only the range of fractional coordinates from 0.2 to 0.8 along *a* is shown, and H atoms are omitted. **b**, Characteristic building unit of ZIF-62 with four crystallographic independent linkers, including one benzimidazole for imidazole substitution that coordinates tetrahedral Zn^{2+}. Approximate bridging angles are indicated, and they are similar to those of SiO_4 networks of silicate minerals. **c**, Schematic of the membrane-driven DAC (photograph) used for lab-based high-*P* experiments. A ring-shaped membrane is inflated by gas pressure, driving the opposing diamond anvils against each other. A gasket with a 200 μm hole containing the sample material, a ruby sphere and the pressure-transmitting medium is shown in the diagram. **d**, Water-cooled vacuum vessel with Kapton windows that contains an externally resistive-heated, membrane-driven DAC, and part of the X-ray collimator assembly, for simultaneous high-*P*, high-*T* PXRD experiments at a synchrotron light source. The direction of beam is indicated by a red arrow. Credit: Betsa (photograph in **c**).

Pbca space group, and adopts a network topology identical to that of the phosphate minerals variscite[38] and strengite[39], and of $CaGa_2O_4$ (ref. [40]) (Fig. 1a,b). Both the natural phosphates and the synthetic gallate display interesting pressure-induced polymorphism[39,41]. To map out the *P*–*T* phase diagram of ZIF-62, we combined in situ powder X-ray diffraction (PXRD, Diamond Light Source, beamline I15) and optical microscopy at simultaneous high *P* and high *T* with ex situ electron microscopy. We also performed constant-pressure first-principles molecular dynamics (FPMD) simulations to provide insight into the pressure dependence at the molecular level.

Constructing the *P*–*T* phase diagram of ZIF-62

A resistively heated membrane-driven diamond anvil cell (DAC, Fig. 1c,d) was used to investigate the phase stability of ZIF-62 in a *P*–*T* range from ambient pressure to 8 GPa and from ambient temperature to 450 °C, respectively. A crystalline sample of evacuated ZIF-62 was loaded into the DAC together with high-purity silicone oil as a non-penetrating, pressure-transmitting medium. In situ characterization of the *P*–*T* evolution of crystalline ZIF-62 was performed with three separate synchrotron- and one lab-based PXRD experiment. The amorphization of ZIF-62 was tracked by observing the loss of diffraction peaks (Supplementary Figure 19). Lab-based optical microscopy was performed to visually determine melting points. The resulting stability fields of crystalline, solid-amorphous and liquid ZIF-62 are shown in Fig. 2a. Solid-state amorphization and melt formation were differentiated by morphological observations of quenched and recovered material (Fig. 2b–d).

Crystalline to solid-amorphous boundary

At ambient *P*, the ZIF-62 structure underwent *T*-induced amorphization at ~320 °C (Fig. 2a), which is in good agreement with a previous study[32]. At high *P* and ambient *T*, the framework underwent amorphization at ~5 GPa. In comparison, a topologically identical structure containing only the unsubstituted imidazolate ligand, ZIF-4, undergoes reversible *P*-induced amorphization at ~1 GPa (ref. [42]). This substantial difference in high-*P* stability at ambient *T* between these two ZIFs may be explained by the more sterically hindered benzimidazolate linkers present in ZIF-62, which protrude into the pore cavities and offer greater stabilization against framework collapse. Force-field-based molecular dynamics simulations

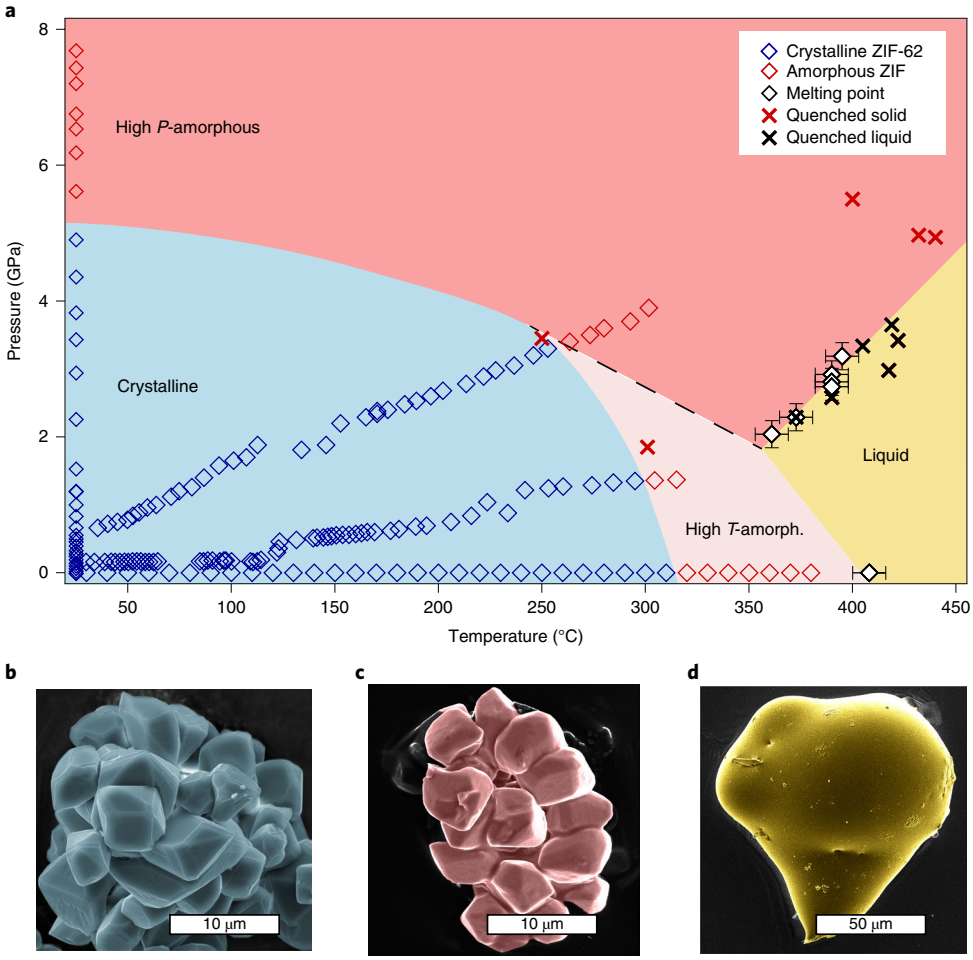

Fig. 2 | Experimentally derived *P*–*T* phase diagram for ZIF-62. a, The stability field of crystalline ZIF-62 is shown in blue, tracing the results of the phase transition analysis from PXRD (blue and red diamonds). Two distinct amorphous phases with high and low densities relative to each other are shaded dark red (high *P*) and light red (high *T*), respectively. This distinction is based on changing slopes of both crystalline–amorphous and solid–liquid phase boundaries. The phase boundary between the two amorphous phases is tentatively indicated with a dashed black line. The phase field for liquid ZIF-62 is shown in yellow, defined by melting points observed optically at high *P* and using DSC at ambient *P*. Crosses indicate high-*P*/high-*T* conditions from which the samples were quenched for morphological analysis. **b**–**d**, Scanning electron microscope images of the three main phases of ZIF-62, in false colours corresponding to those of the stability fields: crystalline, as-synthesized, ZIF-62 (**b**), high-*P* amorphous, quenched from 440 °C, 5 GPa (**c**) and high-*P* molten, quenched from 420 °C, 3.4 GPa (**d**).

of the elastic properties of ZIF-62 and ZIF-4 highlight this structural stabilization: the results (Supplementary Tables 1 and 2) demonstrate higher bulk (4.7 GPa), Young's (8.7 GPa) and shear (3.6 GPa) moduli in ZIF-62 than in ZIF-4 (2.7 GPa, 5.6 GPa and 2.4 GPa, respectively).

P- and *T*-induced amorphization in ZIF-62 were found to be distinct in nature. A synchrotron high-*P* PXRD experiment demonstrated amorphization to occur at 5 GPa. This amorphous phase reverted to the starting crystalline phase on decompression, and the amorphization is thus ascribed to a displacive transition (Fig. 2a, Supplementary Fig. 2). Further evidence for this was uncovered by in situ Raman spectroscopy: the loss of all modes on compression was fully reversed following decompression (Supplementary Fig. 1). Similarly, the related ZIF-4 also undergoes reversible pressure-induced amorphization[42]. In contrast, thermal amorphization of ZIF-62 is irreversible, and thus ascribed to a reconstructive phase transition. Diffraction patterns from samples of ZIF-62 amorphized at (1) 7.6 GPa and 25 °C and (2) 350 °C under vacuum show complete loss of all diffraction peaks in each case (Supplementary Fig. 3).

Amorphization at simultaneous high *P* and high *T* is therefore expected to share aspects of both processes. Moreover, the changing gradient of the crystalline to solid-amorphous transition (Fig. 2a) found across *P*–*T* space is indicative of high-*P* and high-*T* amorphous phases with different densities. This can be derived from the $\Delta S/\Delta V$ term of the Clausius–Clapeyron relation for a boundary with a changing gradient as opposed to one with a constant gradient.

We denote the high-*P* and high-*T* amorphous phases a_{HP} and a_{HT}, and the corresponding crystalline-amorphous transitions c–a_{HP} and c–a_{HT}, respectively. The difference in the slopes of the transitions dominated by either c–a_{HP} or c–a_{HT} in *P*–*T* space implies that $\Delta V_{c-a_{HT}} < \Delta V_{c-a_{HP}}$ and consequently, we find that a_{HP} has a higher density than a_{HT}, as anticipated under the influence of pressure. We defined an approximate boundary between a_{HT} and a_{HP} by extrapolating the c–a_{HP} boundary to higher pressures (dashed line in Fig. 2a).

Solid-amorphous to liquid boundary

The melting point of ZIF-62 at ambient *P* was identified at ~430 °C by differential scanning calorimetry (DSC) measurements (Supplementary Fig. 4). Melting points at high pressures

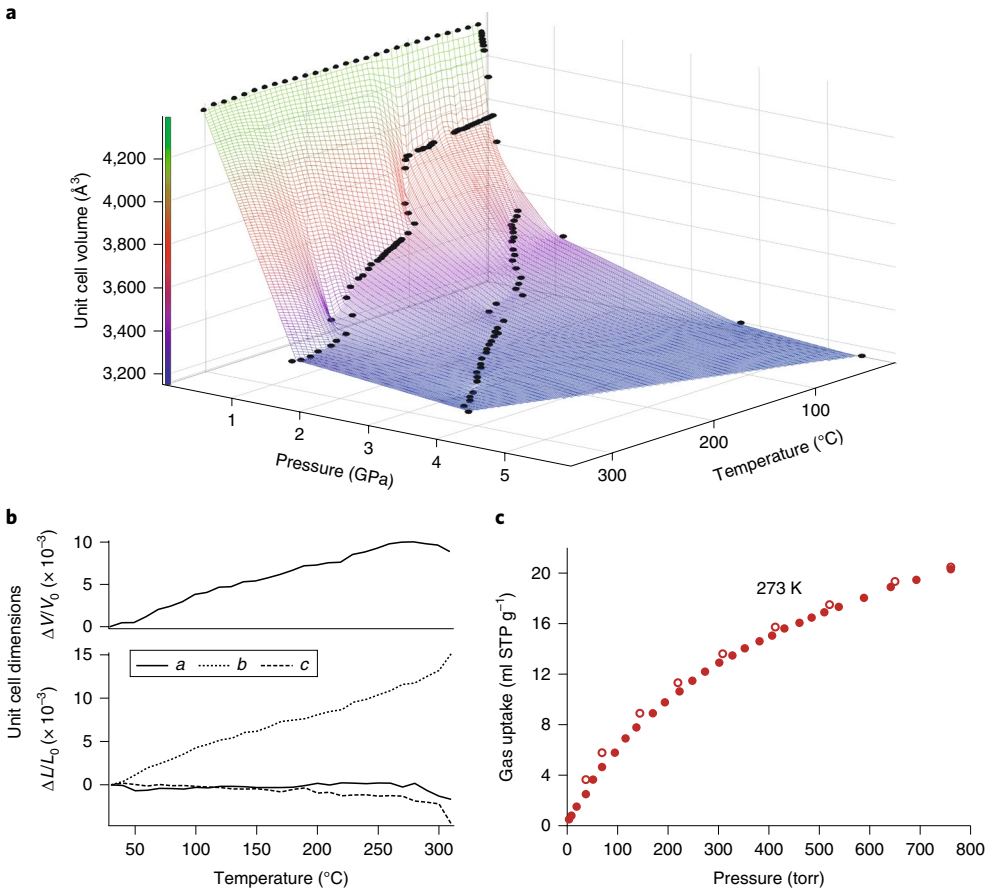

Fig. 3 | Structural evolution of ZIF-62 in *P*–*T* space. a, Unit cell volume of crystalline ZIF-62 as a function of *P* and *T* from Rietveld refinements. A graphically interpolated surface is included as a guide to the eye. **b**, Thermal expansion under vacuum, which is indiscernible on the scale of hydrostatic compression, plotted as relative and normalized change. *L*, unit cell lengths; L_0, unit cell lengths at ambient temperature; *V*, unit cell volume; V_0, unit cell volume at ambient temperature. Top, a volume collapse precedes complete amorphization above 270 °C. Bottom, strong anisotropic expansion is apparent from the individual crystallographic axes. **c**, CO_2 gas adsorption isotherm for the ambient pressure melt-quenched ZIF-62 glass, a_gZIF-62. Filled symbols represent adsorption, open symbols represent desorption.

ranging from approximately 2 GPa to 3.5 GPa were determined visually and are shown in Fig. 2a. A representative video showing the melting is shown in Supplementary Video 1. Six independently determined melting points at variable *P* were fitted linearly with a slope of $dP/dT = 0.031 \pm 0.004$. Achievable *P*–*T* conditions in DAC experiments are constrained to lie on isochores dictated by the properties of the pressure-transmitting medium. For this reason, it was not technically feasible to target *P*–*T* conditions for intermediate *P* and high *T*. However, we are able to constrain the upper limit of the melting curve up to approximately 5 GPa using solids that were quenched from high-*P*, high-*T* conditions indicated in Fig. 2a by red crosses that show no morphological signs of melting (Fig. 2c).

The negative slope of the melting curve interpolated from ambient pressure to <2 GPa (the boundary between light red and yellow in Fig. 2a) implies a solid phase with lower density than the liquid phase. At $P > 2$ GPa, we find a melting curve with a positive gradient (the boundary between dark red and yellow in Fig. 2a), implying the opposite: a solid phase with a higher density than the liquid phase. Both conditions are in accordance with, and support, our model of two distinct amorphous phases a_{HT} and a_{HP}. The intersection of the low- and high-*P* melting curves with the assumed boundary between a_{HT} and a_{HP} (dashed line in Fig. 2a) defines a triple point.

Structural evolution

Temperature- and *P*-dependent lattice parameters of crystalline ZIF-62 were refined from synchrotron and lab-based PXRD data. Figure 3a displays the unit cell volume of ZIF-62 in *P*–*T* space. Purely *P*- and *T*-dependent unit cell dimensions are shown in Fig. 3 and Supplementary Fig. 5, respectively. Experimentally derived bulk moduli and linear thermal expansion coefficients are given in Supplementary Tables 3 and 4. Following quasilinear thermal volume expansion on heating from ambient *T* up to 270 °C—consistent with computational work indicating positive thermal expansion for ZIFs of cag topology[43]—a substantial volume collapse was observed between 270 °C, and complete amorphization at 320 °C (Fig. 3b). This collapse of the unit cell volume coincides with a decrease in diffraction intensity and is due to the transformation to a higher-density phase. On hydrostatic compression at ambient temperature, the *c* axis is the least compressible direction. Under vacuum, thermal expansion is net-zero along the *c* axis, slightly negative along the *a* axis and strongly positive along the *b* axis. This extreme anisotropic behaviour can be understood from the topology of the rings formed by interconnected Zn sites (Supplementary Figs. 6 and 7).

The structure of melt-quenched ZIF-62 has previously been investigated by X-ray total scattering[32]. It was found that the Zn–N association is virtually identical between the crystalline precursor and melt-quenched glass. Permanently porous glasses are rare.

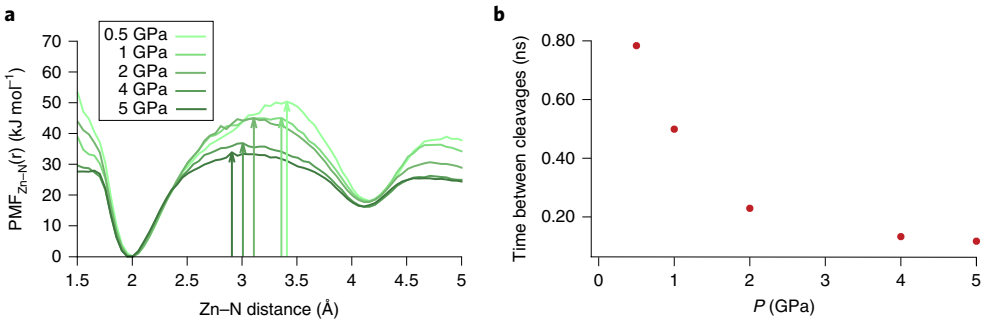

Fig. 4 | Potential of mean force for the Zn–N distance (*r*), and dynamics of Zn–N cleavages. a. Potential of mean force (PMF) for the Zn–N distance, obtained from FPMD of ZIF-62 at pressures between 0.1 GPa and 5 GPa, at a temperature of 1,200 K. The values of the free energy barrier $\Delta G^{\neq}$ corresponding to the breaking of the Zn–N coordination bond (vertical arrows) are given in Table 2. **b**, Time between events of cleavage in a given Zn–N bond as a function of pressure, averaged from the FPMD trajectories.

Table 1 | Gas uptake measured by adsorption isotherms

Gas		H_2	CO_2	O_2	N_2
Kinetic diameter (Å)		**2.9**	**3.3**	**3.46**	**3.64**
Temperature (K)		**77**	**273**	**273**	**77**
Gas uptake (ml STP g^{-1})	ZIF-62	130	39	7.1	0
	a_gZIF-62	9.3	20.1	1.5	0

Uptake was measured at a pressure of 1 bar.

Where they do exist, the porosity in these materials is typically generated by post-synthetic chemical or physical treatments. Conversely, we have recently demonstrated that glasses derived from MOFs can be made permanently accessible to incoming guest molecules such as CO_2 and CH_4 (ref. [36]). Gas adsorption isotherms were used to identify and characterize the accessible pores of crystalline ZIF-62, and the glass formed, hereby referred to as a_gZIF-62, by quenching from the melting point (T_m) at ambient pressure. Crystalline ZIF-62 takes up H_2 at 77 K and CO_2 at 273 K (Supplementary Fig. 8). However, at 77 K, diffusion limitations prevent the ingress of N_2 guest molecules[32]; CH_4 measurements (kinetic diameter 3.8 Å) were also performed to show that this is not a size exclusion effect (Supplementary Fig. 8).

The permanent porosity of a_gZIF-62 was confirmed by recording its uptake of CO_2 at 273 K (Fig. 3c, Table 1). This material reversibly adsorbs 20.1 ml STP g^{-1} at a pressure of 1 bar, which equates to 3.8 wt%. In contrast to the crystalline material, limited uptake of H_2 at 77 K is observed for a_gZIF-62, which is accompanied by substantial hysteresis (Supplementary Fig. 9). This hysteresis is ascribed to diffusion limitations at this temperature, on the basis of the reversibility of the H_2 isotherm measured at 195 K and the CO_2 isotherm measured at 273 K. At 77 K, a small proportion of H_2 cannot be removed in the desorption branch of a_gZIF-62 at very low pressures under practical operating conditions. To confirm that this does not correspond to irreversible chemical modification of a_gZIF-62, the residual gas was removed by warming the sample to room temperature under vacuum. It thus seems that a_gZIF-62 kinetically traps a small amount of H_2, as has been observed in some crystalline systems[44] in which pore openings have similar diameters to the H_2 molecule.

FPMD calculations combined with neutron total scattering data[33] and positron annihilation lifetime spectroscopy[45] have also shown that both the liquid and the quenched glass of ZIF-4 retain porous characteristics similar to the crystalline phase. Here, ex situ Raman spectra of high-*P*, melt-quenched ZIF-62 (Supplementary Fig. 10) are very similar to those of the crystalline starting material, with all Raman modes associated both with the phonon frequencies (<300 cm^{-1}) and the internal modes of organic linkers (>300 cm^{-1}) observed. The only notable difference between the crystalline and the melt-quenched materials is the smoothing of the continuum at wavenumbers <300 cm^{-1}.

A second, high-*P*, high-*T* synchrotron experiment was carried out using ZIF-4 (Supplementary Fig. 11). At ambient *P*, amorphization, recrystallization to the dense ZIF-zni phase and melting were confirmed at ~250 °C, 320 °C and 580 °C, respectively, as expected[34]. However, the application of pressure resulted in a lowering of amorphization and recrystallization temperatures to <200 °C and ~250 °C, respectively, and melting was observed at high pressures below T_m. This hints at transferability in the pressure-induced, lower-temperature melting phenomenon.

Molecular simulations

To give microscopic and thermodynamic insight into the evolution of the ZIF melting processes on application of pressure, we performed FPMD simulations based on a quantum chemical description of the system at the density functional theory level, detailed in the Supplementary Methods. These simulations were performed on both ZIF-4 and ZIF-62, in the 0–5 GPa pressure range at the previously identified computational melting point (for ZIF-4) of 1,200 K (ref. [33]). Given the limited timescale attainable through FPMD simulations, these simulations probe the melting behaviour of the crystalline phase near the experimentally determined crystalline/high-*T*-amorphous and high-*T*-amorphous/liquid phase transitions.

Analysis of the FPMD simulations suggests that the mechanism behind the melting of the ZIFs is not substantially affected by pressure. On the other hand, the application of pressure in the gigapascal range affects both the dynamics and thermodynamics of the systems. Figure 4a depicts the potential of mean force for the Zn–N coordination, calculated from the free FPMD simulations of ZIF-62 at various pressures. There is a clear decrease in the free energy barrier when the pressure is increased from 0.1 GPa to 5 GPa, associated with the rupture of the coordination bond (Table 2, Supplementary Table 5). This can be linked to the softening of the Im–Zn–Im angle on pressurization, which was previously shown to be the driving force of the pressure-induced amorphization of ZIF-8 and ZIF-4 at room temperature[43,46]. Confirmation of this behaviour is also found in the dynamics of the Zn–N coordination bonds, for which the average time between Zn–N cleavage events during the FPMD is shown in Fig. 4b. This softening of the porous framework's coordination on pressurization means that melting becomes thermodynamically easier on application of pressure, explaining the observed negative slope of the ZIF-62 melting curve in *P*–*T* space.

Table 2 | Evolution of the Zn–N coordination $\Delta G^{\neq}$ in ZIF-62 with pressure of ZIF-62

Pressure (GPa)	0.5	1.0	2.0	4.0	5.0
$\Delta G^{\neq}$ (kJ mol^{-1})	50	45	45	37	34

Simulations were also carried out using the published structural model for ZIF-4, producing similar results (Supplementary Fig. 12) and reinforcing the idea that the pressure-induced lowering of the melting point can be generalized to other ZIFs—in a similar way to the pressure-induced amorphization mechanism[46].

This is a counterintuitive behaviour, as for most solids the application of pressure inhibits melting. This raises the possibility that the liquid–solid phase relations of amorphous ZIFs share similarities with those of other disordered framework materials such as H_2O ice. Negative melting curves have also been inferred from separate ambient-T and ambient-P experiments on inorganic zeolites[47], although it is important to note that these deal with collapse of the crystalline state to amorphous solid states, and not to macroscale liquids, as in this study.

There is a large difference in chemistry between ZIFs and zeolites, specifically the weaker Zn–N bonding compared to Si–O interactions[48]. This facilitates melting to a liquid at accessible temperatures and allows us to perform the high-P, high-T experiments required to confirm the negative melting behaviour in these materials.

In contrast, the Zn–N bond is stronger than the interactions present in organic ionic liquids[49], and results not only in higher melting points of ZIFs, but also in a different mechanism of melting. For example, whereas melting in examples of ionic liquids has been shown to result in the complete conformational freedom of component species[50], and molten salt structures such as $ZnCl_2$ have been shown to retain tetrahedral, or octahedral coordination[51], the melting of a ZIF does not result in fully undercoordinated Zn^{2+} centres or $Zn(Im)_4$ fragments[33], but in a strongly associated liquid—once again, similar to liquid water.

Outlook

The P–T phase diagram of the MOFs ZIF-4 and ZIF-62 have been created by combining in situ PXRD and optical microscopy with thermodynamic considerations. Importantly, we show how the stability field of the liquid phase extends substantially towards lower temperatures at increasing hydrostatic pressure. Aside from the fundamental interest in negative-Clapeyron-slope melting behaviour displayed here, reducing the melting temperature is an important objective in developing new MOF glasses. We have also demonstrated the permanent accessible porosity of a_gZIF-62, which will encourage others to research porous glasses, as these compounds decompose at temperatures below their potential melting temperatures[33]. The possibility of synthesizing liquid MOF states via high-P thermal melting opens a route to synthesis of a wide range of amorphous MOFs. The pressure regime required for lowering the melting temperatures is achievable through industrially viable processes such as hot-pressing and specialized autoclaves.

The exploration of P–T space here also provides essential information on the stability of individual phases and the nature of transformations between those phases. The density contrast delineated between high-P and high-T amorphous MOF phases confirms distinct amorphization mechanisms and implies the existence of a point of coexistence between these two amorphous phases and the crystalline state. For example, P- or T-induced transitions have been found in non-ZIF MOFs such as PCN-250 (ref. [52]) and $[NH_4][Zn(HCOO)_3]$ (ref. [53]). This hints at the potential for rich phase diagrams in the MOF family, even at relatively low temperatures and pressures.

Finally, the study of MOFs under simultaneous high P and high T ultimately links polymer chemistry with mineralogy. Tools that are typically used for non-ambient studies in mineral sciences have been adapted for the MOF field, which provides a compelling new perspective on MOFs, and draws parallels between their rich phase-transition behaviour and that of classical inorganic solids such as SiO_2.

Online content

Any methods, additional references, Nature Research reporting summaries, source data, statements of data availability and associated accession codes are available at https://doi.org/10.1038/s41563-019-0317-4.

Received: 18 June 2018; Accepted: 8 February 2019;
Published online: 18 March 2019

References

1. Moghadam, P. Z. et al. Development of a cambridge structural database subset: a collection of metal-organic frameworks for past, present, and future. *Chem. Mater.* **29**, 2618–2625 (2017).
2. Kim, H. et al. Water harvesting from air with metal-organic frameworks powered by natural sunlight. *Science* **356**, 430–434 (2017).
3. Mason, J. A. et al. Methane storage in flexible metal–organic frameworks with intrinsic thermal management. *Nature* **527**, 357–361 (2015).
4. Denny, M. S. Jr, Moreton, J. C., Benz, L. & Cohen, S. M. Metal–organic frameworks for membrane-based separations. *Nat. Rev. Mater.* **1**, 16078 (2016).
5. Mondloch, J. E. et al. Destruction of chemical warfare agents using metal–organic frameworks. *Nat. Mater.* **14**, 512–516 (2015).
6. Horike, S., Shimomura, S. & Kitagawa, S. Soft porous crystals. *Nat. Chem.* **1**, 695–704 (2009).
7. Dissegna, S., Epp, K., Heinz, W. R., Kieslich, G. & Fischer, R. A. Defective metal-organic frameworks. *Adv. Mater.* **30**, 1704501–1704524 (2018).
8. Schneemann, A. et al. Flexible metal-organic frameworks. *Chem. Soc. Rev.* **43**, 6062–6096 (2014).
9. Bennett, T. D., Cheetham, A. K., Fuchs, A. H. & Coudert, F. X. Interplay between defects, disorder and flexibility in metal–organic frameworks. *Nat. Chem.* **9**, 11–16 (2016).
10. Panda, T. et al. Mechanical alloying of metal-organic frameworks. *Angew. Chem. Int. Ed.* **56**, 2413–2417 (2017).
11. Coudert, F.-X. responsive metal–organic frameworks and framework materials: under pressure, taking the heat, in the spotlight, with friends. *Chem. Mater.* **27**, 1905–1916 (2015).
12. Krause, S. et al. A pressure-amplifying framework material with negative gas adsorption transitions. *Nature* **532**, 348–352 (2016).
13. Carrington, E. J. et al. Solvent-switchable continuous-breathing behaviour in a diamondoid metal–organic framework and its influence on CO_2 versus CH_4 selectivity. *Nat. Chem.* **9**, 882–889 (2017).
14. Longley, L., Li, N., Wei, F. & Bennett, T. D. Uncovering a reconstructive solid–solid phase transition in a metal–organic framework. *R. Soc. Open Sci.* **4**, 171355 (2017).
15. Lapidus, S. H., Halder, G. J., Chupas, P. J. & Chapman, K. W. Exploiting high pressures to generate porosity, polymorphism, and lattice expansion in the nonporous molecular framework $Zn(CN)_2$. *J. Am. Chem. Soc.* **135**, 7621–7628 (2013).
16. Robert M. Hazen, R. T. D. *High-Temperature and High-Pressure Crystal Chemistry* (Reviews in Mineralogy and Geochemistry Vol. 41, Mineralogical Society of America, 2003).
17. Dove, M. T. et al. Crystal structure of the high-pressure monoclinic phase-II of cristobalite, SiO_2. *Mineral. Mag.* **64**, 569–576 (2000).
18. Hemley, R. J., Jephcoat, A. P., Mao, H. K., Ming, L. C. & Manghnani, M. H. Pressure-induced amorphization of crystalline silica. *Nature* **334**, 52–54 (1988).
19. Natarajan, S. & Mahata, P. Metal-organic framework structures - how closely are they related to classical inorganic structures? *Chem. Soc. Rev.* **38**, 2304–2318 (2009).
20. Decurtins, S., Schmalle, H. W., Schneuwly, P., Ensling, J. & Guetlich, P. A concept for the synthesis of 3-dimensional homo-and bimetallic oxalate-bridged networks $[M_2(ox)_3]_n$. Structural, Moessbauer, and magnetic studies in the field of molecular-based magnets. *J. Am. Chem. Soc.* **116**, 9521–9528 (1994).
21. Sadakiyo, M., Yamada, T., Honda, K., Matsui, H. & Kitagawa, H. Control of crystalline proton-conducting pathways by water-induced transformations of hydrogen-bonding networks in a metal–organic framework. *J. Am. Chem. Soc.* **136**, 7701–7707 (2014).

22. Huskić, I., Pekov, I. V., Krivovichev, S. V. & Friščić, T. Minerals with metal-organic framework structures. *Sci. Adv.* **2**, e1600621–e1600629 (2016).
23. Banerjee, R. et al. High-throughput synthesis of zeolitic imidazolate frameworks and application to CO_2 capture. *Science* **319**, 939–943 (2008).
24. Park, K. S. et al. Exceptional chemical and thermal stability of zeolitic imidazolate frameworks. *Proc. Natl Acad. Sci. USA* **103**, 10186–10191 (2006).
25. McKellar, S. C. & Moggach, S. A. Structural studies of metal-organic frameworks under high pressure. *Acta Crystallogr. Sect. B* **71**, 587–607 (2015).
26. Cruciani, G. Zeolites upon heating: factors governing their thermal stability and structural changes. *J. Phys. Chem. Solids* **67**, 1973–1994 (2006).
27. Hazen, R. M. Zeolite molecular sieve 4A: anomalous compressibility and volume discontinuities at high pressure. *Science* **219**, 1065–1067 (1983).
28. Chapman, K. W., Sava, D. F., Halder, G. J., Chupas, P. J. & Nenoff, T. M. Trapping guests within a nanoporous metal–organic framework through pressure-induced amorphization. *J. Am. Chem. Soc.* **133**, 18583–18585 (2011).
29. Zhao, P. et al. Pressure-induced oversaturation and phase transition in zeolitic imidazolate frameworks with remarkable mechanical stability. *Dalt. Trans.* **44**, 4498–4503 (2015).
30. Henke, S. et al. Pore closure in zeolitic imidazolate frameworks under mechanical pressure. *Chem. Sci.* **9**, 1654–1660 (2018).
31. Bennett, T. D. et al. Thermal amorphization of zeolitic imidazolate frameworks. *Angew. Chemie Int. Ed.* **50**, 3067–3071 (2011).
32. Bennett, T. D. et al. Melt-quenched glasses of metal–organic frameworks. *J. Am. Chem. Soc.* **138**, 3484–3492 (2016).
33. Gaillac, R. et al. Liquid metal–organic frameworks. *Nat. Mater.* **16**, 1149–1155 (2017).
34. Bennett, T. D. et al. Hybrid glasses from strong and fragile metal-organic framework liquids. *Nat. Commun.* **6**, 8079–8086 (2015).
35. Qiao, A. et al. A metal-organic framework with ultrahigh glass-forming ability. *Sci. Adv.* **4**, 6827–6834 (2018).
36. Zhou, C. et al. Metal-organic framework glasses with permanent accessible porosity. *Nat. Commun.* **9**, 5042–5051 (2018).
37. Wenqian, C. et al. Glass formation of a coordinationpolymer crystal for enhanced proton conductivity and material flexibility. *Angew. Chemie Int. Ed.* **55**, 5195–5200 (2016).
38. Kniep, R., Mootz, D. & Vegas, A. Variscite. *Acta Crystallogr.* **B33**, 263–265 (1977).
39. Song, Y., Zavalij, P. Y., Suzuki, M. & Whittingham, M. S. New iron(III) phosphate phases: crystal structure and electrochemical and magnetic properties. *Inorg. Chem.* **41**, 5778–5786 (2002).
40. Deiseroth, H. J. & Müller -Buschbaum, H. Über Erdalkalimetalloxogallate. III: Untersuchung des Aufbaus von CaGa O . *Z. Anorg. Allg. Chem.* **396**, 157–164 (1973).
41. Lazić, B., Kahlenberg, V. & Konzett, J. Rietveld analysis of a high pressure modification of monocalcium oxogallate ($CaGa_2O_4$). *Z. Anorg. Allg. Chem.* **631**, 2411–2415 (2005).
42. Bennett, T. D. et al. Reversible pressure-induced amorphization of a zeolitic imidazolate framework (ZIF-4). *Chem. Commun.* **47**, 7983–7985 (2011).
43. Bouëssel du Bourg, L., Ortiz, A. U., Boutin, A. & Coudert, F. X. Thermal and mechanical stability of zeolitic imidazolate frameworks polymorphs. *APL Mater.* **2**, 124110–124118 (2014).
44. Yang, S. et al. Cation-induced kinetic trapping and enhanced hydrogen adsorption in a modulated anionic metal–organic framework. *Nat. Chem.* **1**, 487–493 (2009).
45. Thornton, A. W. et al. Porosity in metal-organic framework glasses. *Chem. Commun.* **52**, 3750–3753 (2016).
46. Ortiz, A. U., Boutin, A., Fuchs, A. H. & Coudert, F.-X. Investigating the pressure-induced amorphization of zeolitic imidazolate framework ZIF-8: mechanical instability due to shear mode softening. *J. Phys. Chem. Lett.* **4**, 1861–1865 (2013).
47. Greaves, G. N. et al. Zeolite collapse and polyamorphism. *J. Phys. Condens. Matter* **19**, 415102–415119 (2007).
48. Greaves, G. N. & Meneau, F. Probing the dynamics of instability in zeolitic materials. *J. Phys. Condens. Matter* **16**, 3459–3472 (2004).
49. Armand, M., Endres, F., MacFarlane, D. R., Ohno, H. & Scrosati, B. Ionic-liquid materials for the electrochemical challenges of the future. *Nat. Mater.* **8**, 621–629 (2009).
50. Lima, T. A., Paschoal, V. H., Faria, L. F. O. & Ribeiro, M. C. C. Unraveling the stepwise melting of an ionic liquid. *J. Phys. Chem. B* **121**, 4650–4655 (2017).
51. McGreevy, R. L. & Pusztai, L. The structure of molten salts. *Proc. Math. Phys. Sci.* **430**, 241–261 (1990).
52. Yuan, S. et al. PCN-250 under pressure: sequential phase transformation and the implications for MOF densification. *Joule* **1**, 806–815 (2017).
53. Mączka, M. et al. Temperature- and pressure-induced phase transitions in the metal formate framework of $[ND_4][Zn(DCOO)_3]$ and $[NH_4][Zn(HCOO)_3]$. *Inorg. Chem.* **53**, 9615–9624 (2014).

Acknowledgements

R.N.W. acknowledges support from the EPSRC in the form of a DTG Graduate Studentship. R.N.W. and A.M.B. thank C. Hunter and his group, at the Department of Chemistry (University of Cambridge), for the use of their HPLC facilities. T.D.B. thanks the Royal Society for a University Research Fellowship and for their support (UF150021). C.Z. acknowledges the financial support of the Elite Research Travel Scholarship from the Danish Ministry of Higher Education and Science. We thank Diamond Light Source for access to beamline I15 (EE16133 and EE19046-1). This work benefitted from the financial support of ANRT (thèse CIFRE 2015/0268) and access to HPC platforms provided by a GENCI grant (A0050807069). Gas sorption on the ZIF-62 glass was supported by a grant from the National Science Foundation, Division of Chemistry under award number CHE-1661655. Synthesis of MOFs was supported by a grant from the National Science Foundation under award number CHE-1359906 (to S.M.C.). L. Friche, N. Bandata and O. T. Qasvini (Massey Unviersity) are thanked for technical assistance, alongside B. R. Pimentel (UCSD).

Author contributions

T.D.B. and S.A.T.R. designed the project. R.N.W., G.I.L, S.A., S.G.M, A.K.K., M.T.W., S.F., C.Z., C.W. and T.D.B. performed the PXRD experiments. S.G.M. designed and constructed the high-*P*-*T* PXRD equipment. R.N.W. performed melting point determinations, Raman spectroscopy and microscopy, and analysed XRD and spectroscopic data. H.P. and C.Z. performed DSC measurements. A.M.B. and R.N.W. performed HPLC measurements. X.Y, S.M.C. and S.G.T. performed gas sorption measurements. R.G. and F.-X.C. designed, performed and analysed the molecular simulations. All authors participated in discussing the data. R.N.W. and T.D.B. wrote the manuscript with input from all authors.

Competing interests

The authors declare no competing interests.

Additional information

Supplementary information is available for this paper at https://doi.org/10.1038/s41563-019-0317-4.

Reprints and permissions information is available at www.nature.com/reprints.

Correspondence and requests for materials should be addressed to T.D.B.

Publisher's note: Springer Nature remains neutral with regard to jurisdictional claims in published maps and institutional affiliations.

Methods

ZIF-62 and ZIF-4 were prepared and desolvated according to a procedure adapted from the literature[54]. Specifically, ZIF-62 and ZIF-4 were synthesized by a solvothermal method in which 1.515 g $Zn(NO_3)_2{\cdot}6H_2O$ (8 mmol), 7.35 g imidazole (108 mmol) and 1.418 g benzimidazole (12 mmol) (ZIF-62) and 1.2 g $Zn(NO_3)_2{\cdot}6H_2O$ (4.03 mmol) and 0.9 g imidazole (13.2 mmol) (ZIF-4) were dissolved in 75 ml of dimethylformamide and transferred into a 100 ml glass jar. The jars were sealed tightly and heated to 130 °C for 48 h in an oven. The filtered off, as-synthesized ZIFs were soaked in dichloromethane for solvent exchange for 24 hours and subsequently desolvated in a vacuum oven at 0.01 mbar and 140 °C. A sample of a_gZIF-62 was prepared by heating ZIF-62 under argon in a tube furnace to 430 °C, and cooling naturally.

The resulting compositions are $Zn(Im)_{1.76}(bIm)_{0.24}$ for ZIF-62, and $Zn(Im)_2$ for ZIF-4 as determined by high-performance liquid chromatography (HPLC) (Supplementary Methods, Supplementary Fig. 13). The XRD patterns and Raman spectra of the starting materials are shown in Supplementary Fig. 14.

Ambient-pressure, variable-temperature PXRD data were collected under vacuum on a Bruker D8 Advance diffractometer equipped with a radiation-heating stage (MRI Physikalische Geräte GmbH, Germany). Pure silicon powder was mixed with ZIF-62 and ZIF-4 and used as an internal standard for sample displacement corrections.

Combined high-*P* and high-*T* PXRD data for ZIF-62 and ZIF-4 were obtained at beamline I15, Diamond Light Source, Didcot (Supplementary Figs. 15–19). A membrane-driven DAC was equipped with an external coiled resistive heater. The DAC was contained in a water-cooled vacuum vessel with Kapton windows. High-purity silicone oil (AP100, Sigma-Aldrich) was used as pressure-transmitting medium. Data were collected at a wavelength of $\lambda = 0.4246$ Å using a MAR345 detector. Diffraction images were integrated using the DAWN software suite[55]. Internal pressures were calculated from the unit cell volume of NaCl using equation-of-state parameters from literature[56]. A K-type thermocouple with an accuracy of <0.4 % was glued close to one of the diamonds to provide temperature measurements. Before each heating ramp, the internal pressure of the DAC was raised to a target value by inflating the membrane. This membrane pressure was kept constant throughout the individual runs. Temperature was raised continuously at an average rate of 0.5 °C min^{-1} for run 1 and 1 °C min^{-1} for run 2, resulting in simultaneous increases in *T* and *P*. Diffraction patterns were collected at temperature increments of approximately 10 °C.

Melting points of ZIF-62 at high *P* were determined visually from lab-based, externally heated DAC experiments in silicone oil as the pressure-transmitting medium (Supplementary Figs. 20 and 21). Optical images of the recovered ZIF-4 samples are presented in Supplementary Fig. 22. The temperature was measured using a K-type thermocouple glued to one of the diamonds. The pressure was determined from the shift of the fluorescence peaks of ruby[57] corrected for the *T*-induced shift[58]. The temperature was increased continuously at a rate of approximately 5 °C min^{-1}, whereas the initial membrane pressure was kept constant. The lowest possible pressure at a certain temperature is dictated by the isochoric path followed by the increase in *T* . Therefore, it was not possible to access pressures below 2 GPa between 300 °C and 350 °C. After reaching maximum *T* and *P* conditions, the external heater was switched off, resulting in an approximate cooling rate of 2.5 K min^{-1}. The pressure was released after reaching room temperature. The gaskets containing samples were transferred to scanning electron microscopy stubs, kept under vacuum for 48 h to evaporate silicone oil residues and carbon coated for subsequent scanning electron microscope imaging. Back-scattered electron images were acquired on an FEI Qemscan Quanta650F operated at 10 kV at a working distance of 10 mm.

Rietveld refinement of experimental diffraction patterns was performed using TOPAS-Academic v6[59] based on a ZIF-62 and ZIF-4 structure model from the literature[23]. Synchrotron-based PXRD data were fitted sequentially using experimental peak shapes from LaB_6 reference measurements. An experimental, fixed background profile measured from an empty DAC in the vacuum vessel was fitted together with fifth-order Chebychev polynomial. Eighth-order spherical harmonics were applied to intensities for preferred orientation correction. Lattice parameters, scaling factors and Lorentzian strain were refined individually for all measurements. Numeric fit results are presented in the Supplementary Information.

Lab-based, variable-temperature PXRD datasets were fitted parametrically. An internal silicon standard allowed individual sample displacements to be refined using fixed, temperature-dependent standard lattice parameters for silicon at each temperature[60]. ZIF-62 and ZIF-4 were then fitted using the fixed, previously refined, specimen displacements.

Gas adsorption isotherms were measured by a volumetric method using ultrahigh-purity gases. Before analysis, the samples were degassed under a dynamic vacuum at 1×10^{-6} torr for 10–20 h at 130–250 °C. Accurate sample masses were calculated using degassed samples after the sample tubes were backfilled with nitrogen.

Data availability

Experimental and computational data supporting the findings of this work are available from the public GitHub online repository at https://github.com/fxcoudert/citable-data.

References

54. Gustafsson, M. & Zou, X. Crystal formation and size control of zeolitic imidazolate frameworks with mixed imidazolate linkers. *J. Porous Mater.* **20**, 55–63 (2013).
55. Filik, J. et al. Processing two-dimensional X-ray diffraction and small-angle scattering data in DAWN 2. *J. Appl. Crystallogr.* **50**, 959–966 (2017).
56. Dorogokupets, P. I. & Dewaele, A. Equations of state of MgO, Au, Pt, NaCl-B1, and NaCl-B2: Internally consistent high-temperature pressure scales. *High Press. Res.* **27**, 431–446 (2007).
57. Dewaele, A., Torrent, M., Loubeyre, P. & Mezouar, M. Compression curves of transition metals in the mbar range: experiments and projector augmented-wave calculations. *Phys. Rev. B* **78**, 104102–104115 (2008).
58. Rekhi, S., Dubrovinsky, L. S. & Saxena, S. K. Temperature-induced ruby fluorescence shifts up to a pressure of 15 GPa in an externally heated diamond anvil cell. *HighTemp. High Press.* **31**, 299–305 (1999).
59. Coelho, A. A. TOPAS and TOPAS-Academic: an optimization program integrating computer algebra and crystallographic objects written in C++. *J. Appl. Crystallogr.* **51**, 210–218 (2018).
60. Stinton, G. W. & Evans, J. S. O. Parametric Rietveld refinement. *J. Appl. Crystallogr.* **40**, 87–95 (2007).